

**Supplemental Material for “Giant Thermal Enhancement of the  
Electric Polarization in Ferrimagnetic  $\text{BiFe}_{1-x}\text{Co}_x\text{O}_3$  Solid  
Solutions Near Room Temperature”**

César Menéndez

*School of Materials Science and Engineering,  
UNSW Sydney, Sydney, NSW 2052, Australia*

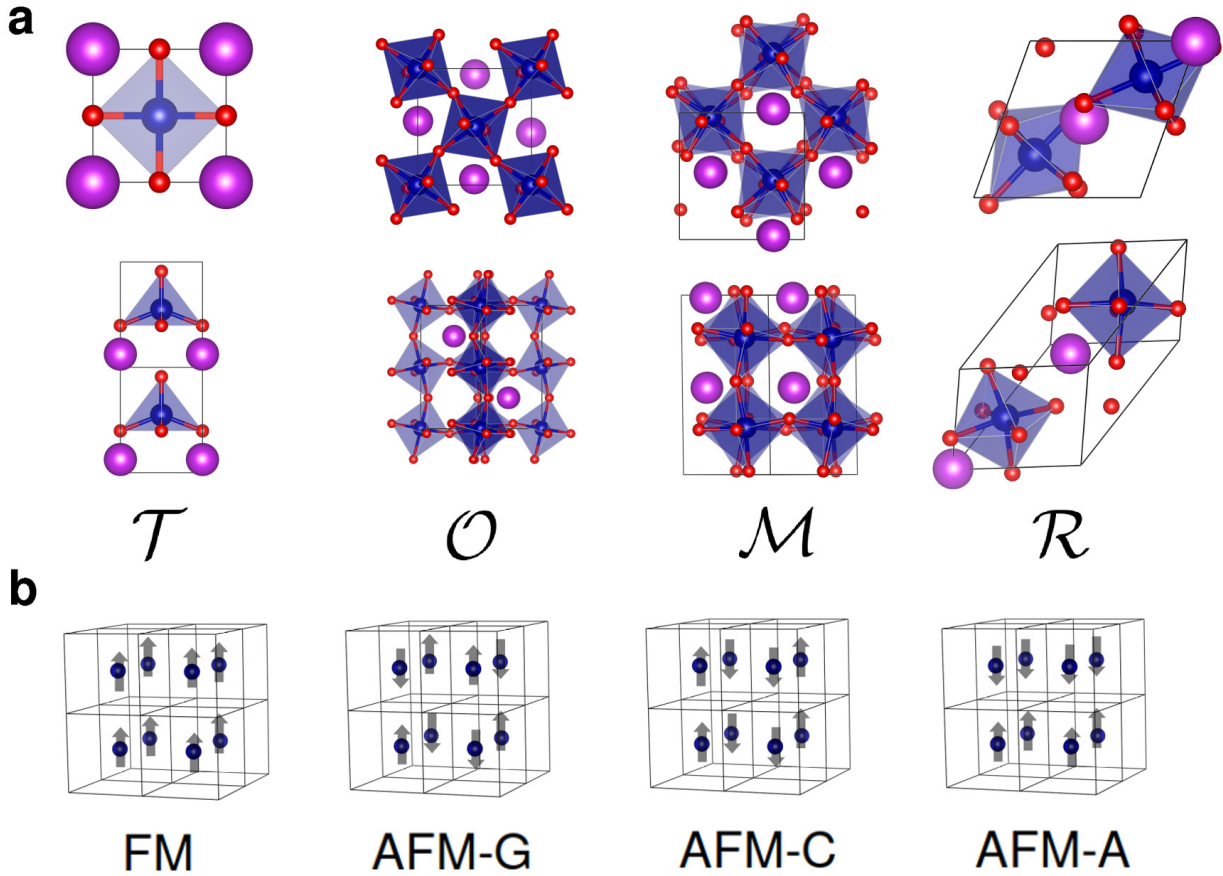
Claudio Cazorla

*Departament de Física, Universitat Politècnica de Catalunya,  
Campus Nord B4-B5, E-08034 Barcelona, Spain*

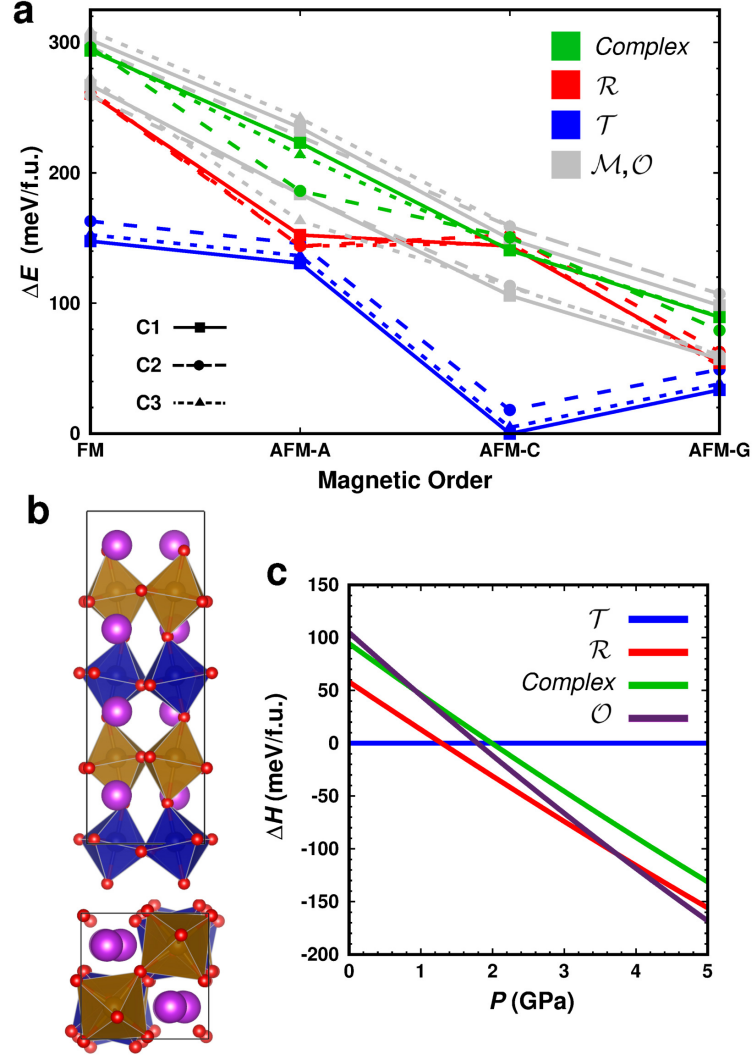
**Abstract**

In this supplemental document, we provide additional details on the structural, vibrational, magnetic, and ferroelectric properties of the bulk phases of  $\text{BiFe}_{1-x}\text{Co}_x\text{O}_3$  solid solutions (cases  $x = 0.5$  and  $0.25$ ) as obtained with first-principles methods based on density functional theory (DFT). The influence of (i) the employed DFT exchange-correlation functional and (ii) the likely existence of non-ergodic cation redistribution effects during the  $\mathcal{T} \leftrightarrow \mathcal{R}$  phase transformation on the main conclusions presented in the main text are also discussed.

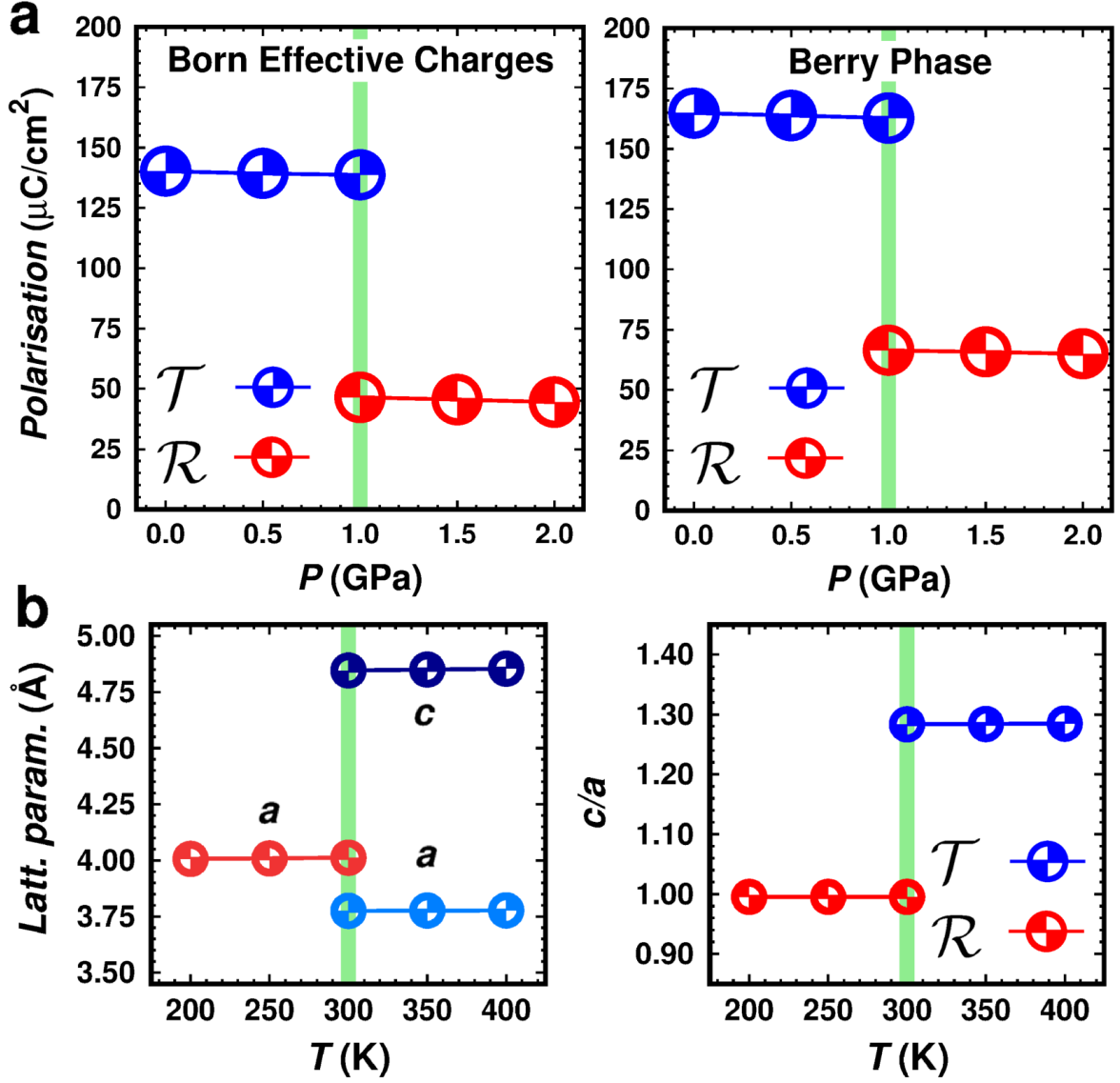
SUPPLEMENTARY FIGURES



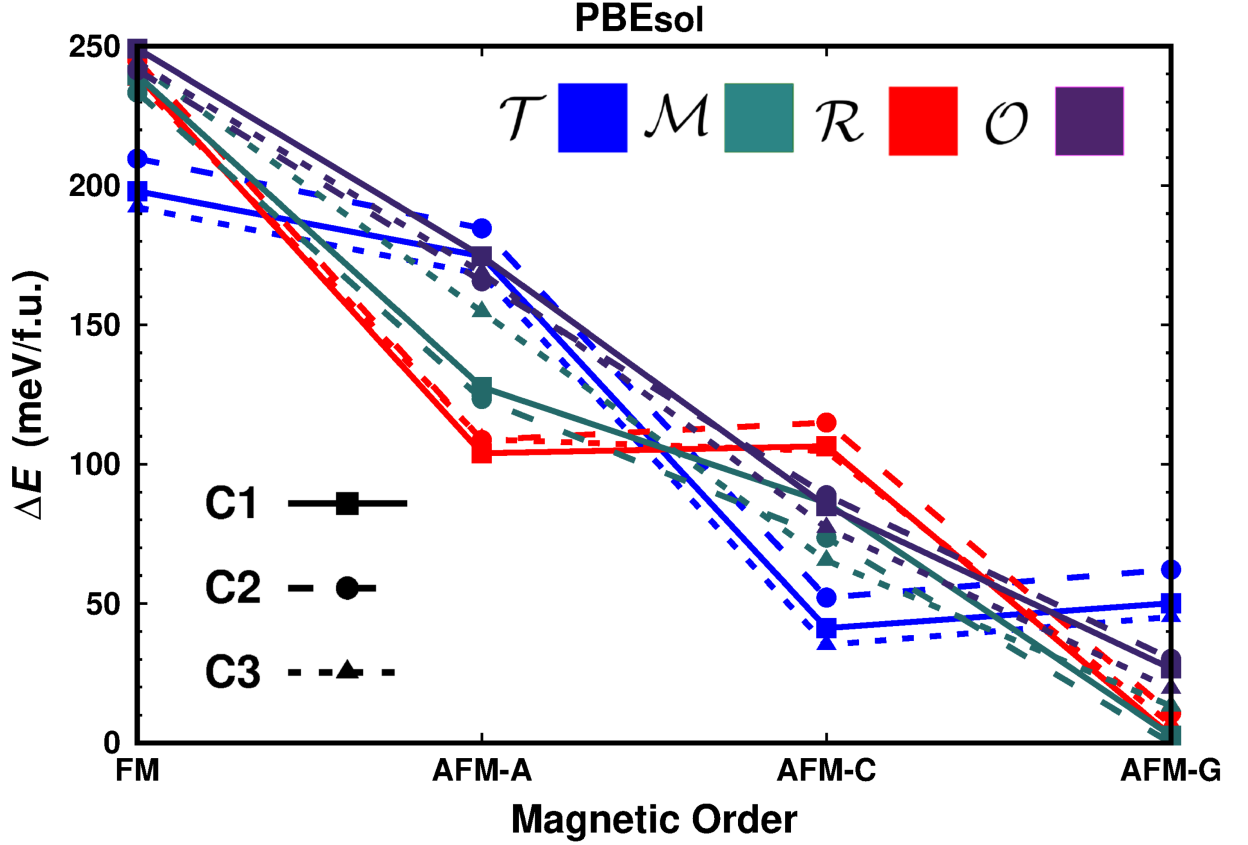
**Supplementary Figure 1:** (a) Representation of the four parent crystal structures considered for bulk  $\text{BiFe}_{1-x}\text{Co}_x\text{O}_3$  solid solutions in this study (based on a previous study by Diéguez and Íñiguez [1]). Transition metal, bismuth and oxygen atoms are represented with blue, violet and red spheres, respectively. (b) Sketch of the four different transition-metal magnetic spin arrangements considered for bulk  $\text{BiFe}_{1-x}\text{Co}_x\text{O}_3$  solid solutions in this study. Grey arrows represent “spin-up” and “spin-down” magnetic orientations in the transition-metal positions forming a simple cubic sublattice.



**Supplementary Figure 2:** Energy results obtained for a recently reported orthorhombic phase that exhibits complex and nano-twinned  $O_6$  tilting patterns [2], labelled here as “Complex”. (a) Energy results obtained for bulk  $\text{BiFe}_{0.5}\text{Co}_{0.5}\text{O}_3$  at zero pressure with the PBE DFT functional [3]. Crystal structures with tetragonal ( $\mathcal{T}$ ), monoclinic ( $\mathcal{M}$ ), rhombohedral ( $\mathcal{R}$ ), and orthorhombic ( $\mathcal{O}$  and “Complex”) symmetry were considered. All possible Co–Fe (C1, C2, and C3 –Fig.1 in the main text–) and magnetic spin arrangements (ferromagnetic –FM– and antiferromagnetic –AFM– of type A, C, and G –Supplementary Fig.1–) were considered. (b) Ball-stick representation of the orthorhombic “Complex” phase. Bi, Fe, Co and O atoms are represented with violet, gold, blue and red spheres, respectively. (c) Zero-temperature enthalpy difference with respect to the  $\mathcal{T}$  phase,  $\Delta H = H_X - H_{\mathcal{T}}$ , expressed as a function of pressure. At low temperatures and  $P \approx 4$  GPa, the orthorhombic  $\mathcal{O}$  becomes the  $\text{BiFe}_{0.5}\text{Co}_{0.5}\text{O}_3$  ground state.

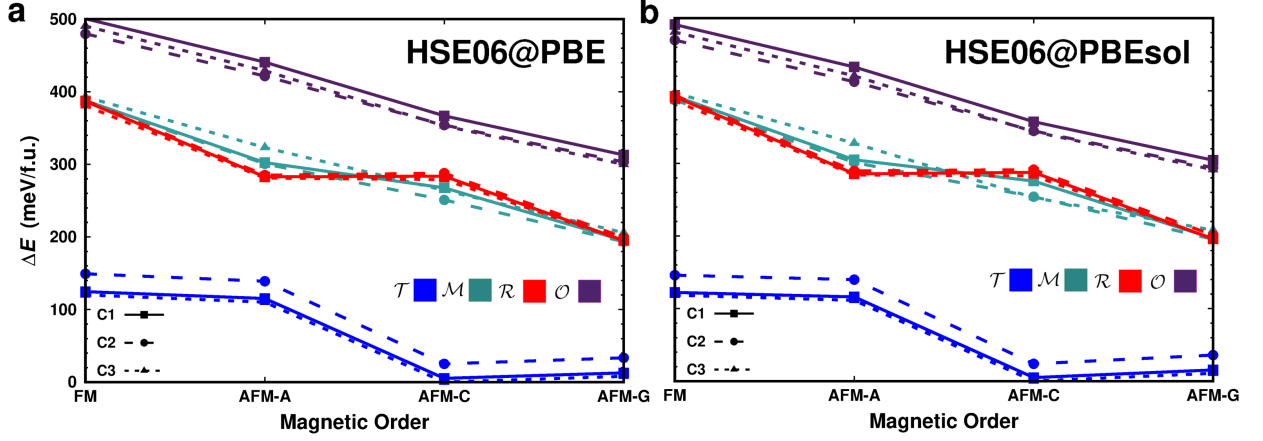


**Supplementary Figure 3:** Electric polarization and structural properties of bulk  $\text{BiFe}_{0.5}\text{Co}_{0.5}\text{O}_3$ . (a) Electric polarization of the  $\mathcal{T}$  and  $\mathcal{R}$  phases calculated with the Born effective charges approach [4] and the Berry phase formalism [5–7] and expressed as a function of pressure. The range-separated hybrid functional introduced by Heyd, Scuseria and Ernzerhof (HSE06) [8] was employed for these calculations. The calculation of the electric polarization was performed at  $T = 0$  conditions however, based on the experimental data reported by Azuma *et al.* [9,10], it is reasonable to expect that the estimated  $p$  values will not be affected noticeably by room-temperature thermal excitations. (b) Structural parameters of the  $\mathcal{T}$  and  $\mathcal{R}$  phases estimated at a pressure of 1.2 GPa and expressed as a function of temperature.

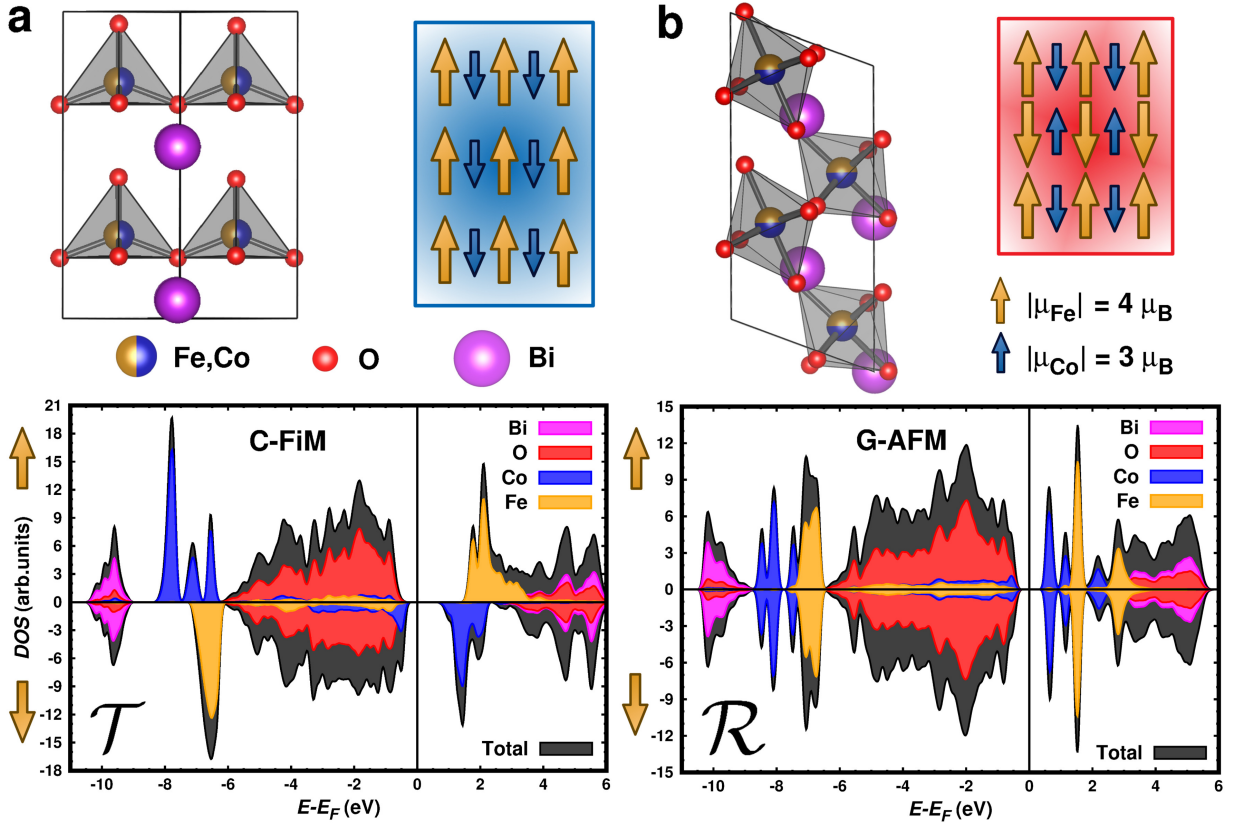


**Supplementary Figure 4:** First-principles analysis of bulk  $\text{BiFe}_{0.5}\text{Co}_{0.5}\text{O}_3$  at zero pressure and  $T = 0$  based on the PBEsol DFT exchange-correlation energy functional [11].

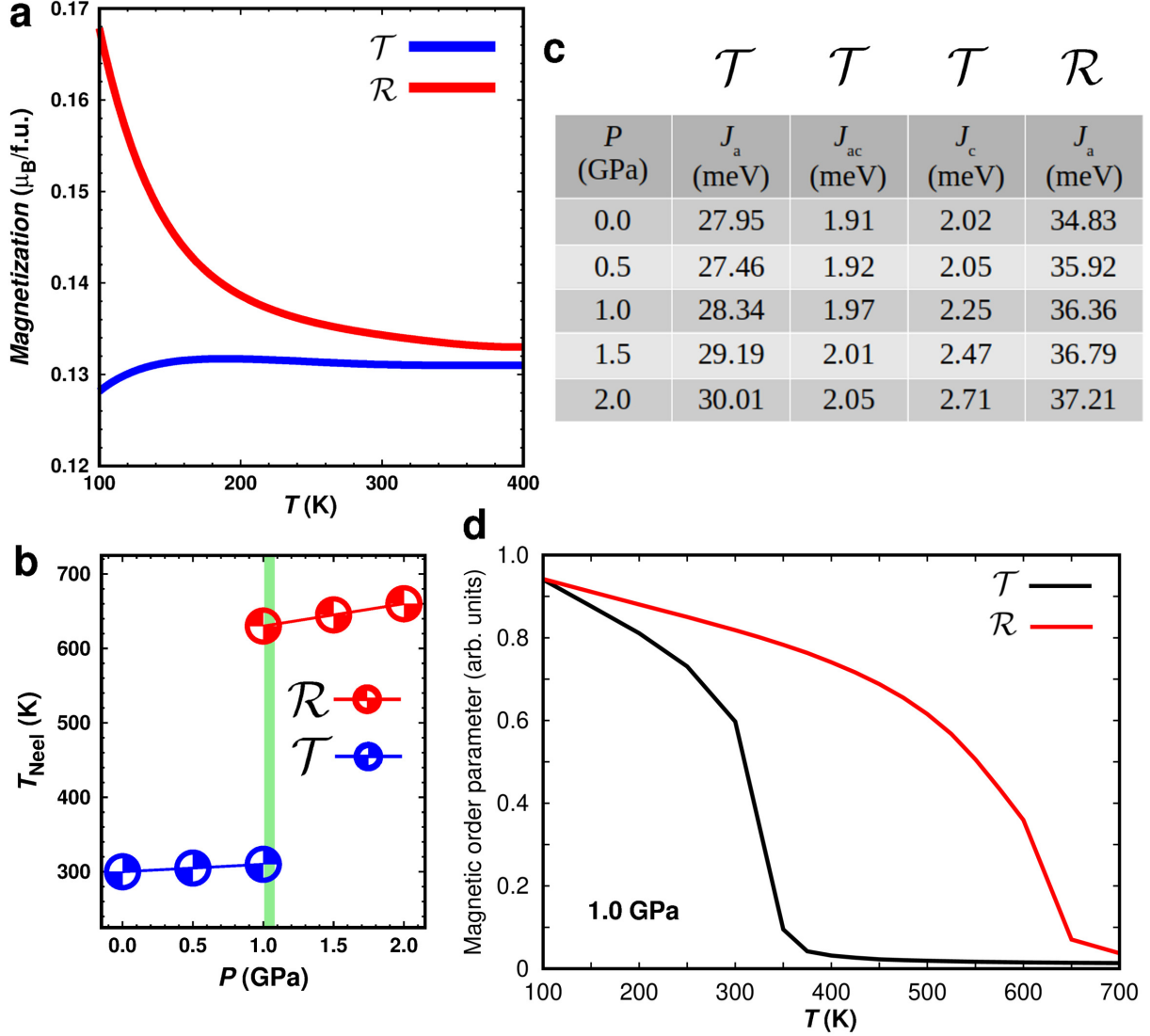
Crystal structures with tetragonal ( $\mathcal{T}$ ), monoclinic ( $\mathcal{M}$ ), rhombohedral ( $\mathcal{R}$ ), and orthorhombic ( $\mathcal{O}$ ) symmetry were considered (Supplementary Fig.1). All possible Co-Fe (C1, C2, and C3 –Fig.1 in the main text–) and magnetic spin arrangements (ferromagnetic –FM– and antiferromagnetic –AFM– of type A, C, and G –Supplementary Fig.1–) were generated for a  $2 \times \sqrt{2} \times \sqrt{2}$  simulation cell containing 20 atoms [4]. The obtained PBEsol results differ appreciably from those estimated with the PBE DFT exchange-correlation energy functional [3] for the same system (Fig.1 in the main text).



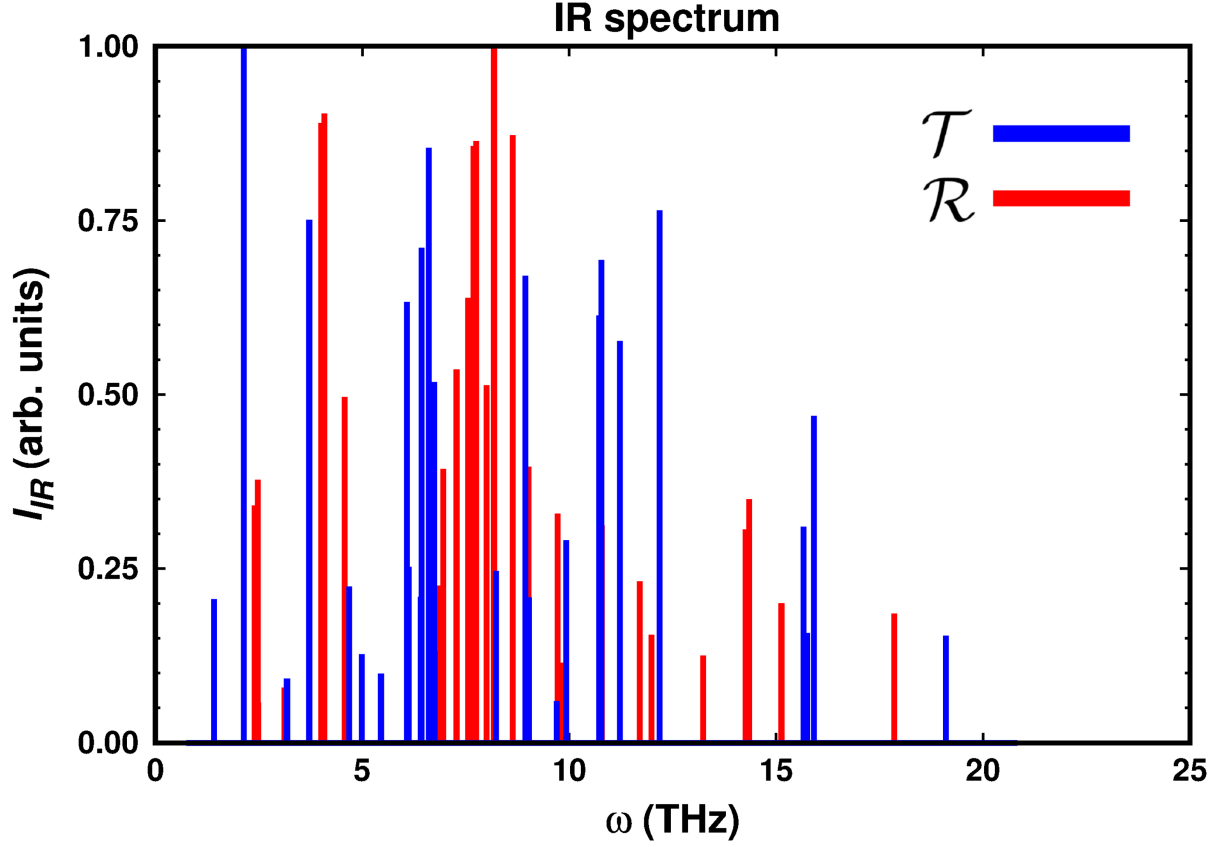
**Supplementary Figure 5:** First-principles analysis of bulk  $\text{BiFe}_{0.5}\text{Co}_{0.5}\text{O}_3$  at zero pressure and  $T = 0$  based on the range-separated hybrid DFT functional HSE06 [8]. Equilibrium geometries are determined with (a) the PBE [3] and (b) PBEsol DFT exchange-correlation energy functionals [11]. Crystal structures with tetragonal ( $\mathcal{T}$ ), monoclinic ( $\mathcal{M}$ ), rhombohedral ( $\mathcal{R}$ ), and orthorhombic ( $\mathcal{O}$ ) symmetry were considered (Supplementary Fig.1). All possible Co–Fe (C1, C2, and C3 –Fig.1 in the main text–) and magnetic spin arrangements (ferromagnetic –FM– and antiferromagnetic –AFM– of type A, C, and G –Supplementary Fig.1–) were generated for a  $2 \times \sqrt{2} \times \sqrt{2}$  simulation cell containing 20 atoms [4]. The obtained HSE06 results are in fairly good agreement with those estimated with the PBE DFT exchange-correlation energy functional [3] for the same system (Fig.1 in the main text).



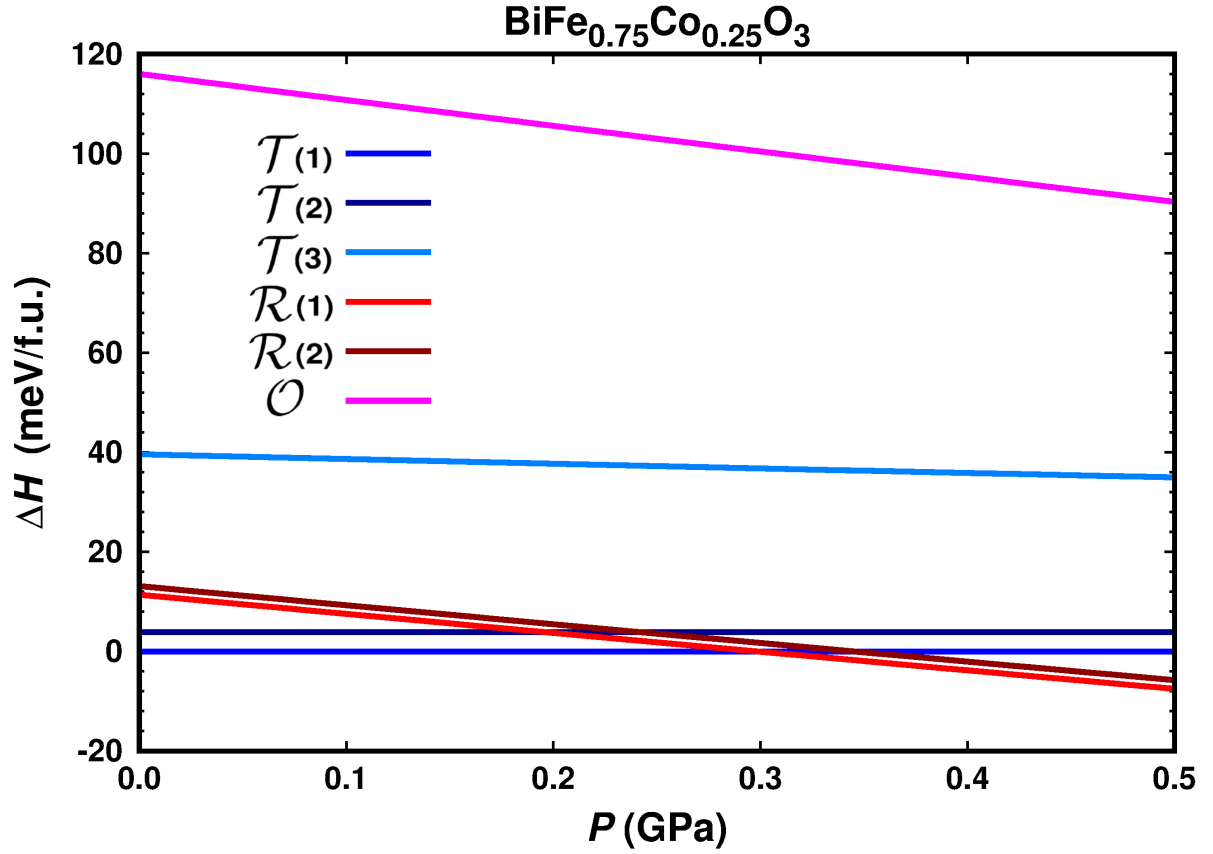
**Supplementary Figure 6:** (a) Structural and magnetic characterization of the  $\mathcal{T}$  phase of bulk  $\text{BiFe}_{0.5}\text{Co}_{0.5}\text{O}_3$  obtained at zero temperature. Yellow and blue arrows indicate the magnetic spin moments of Fe and Co ions, respectively. Projected density of electronic states obtained for a ferrimagnetic (FiM) configuration exhibiting a net magnetization, which results from a spin imbalance between the magnetic Fe and Co ion sublattices. (b) Structural and magnetic characterization of the  $\mathcal{R}$  phase of bulk  $\text{BiFe}_{0.5}\text{Co}_{0.5}\text{O}_3$  obtained at zero temperature. Projected density of electronic states obtained for an antiferromagnetic (AFM) configuration exhibiting a null magnetization, which results from a perfect spin cancellation between the magnetic Fe and Co ion sublattices.



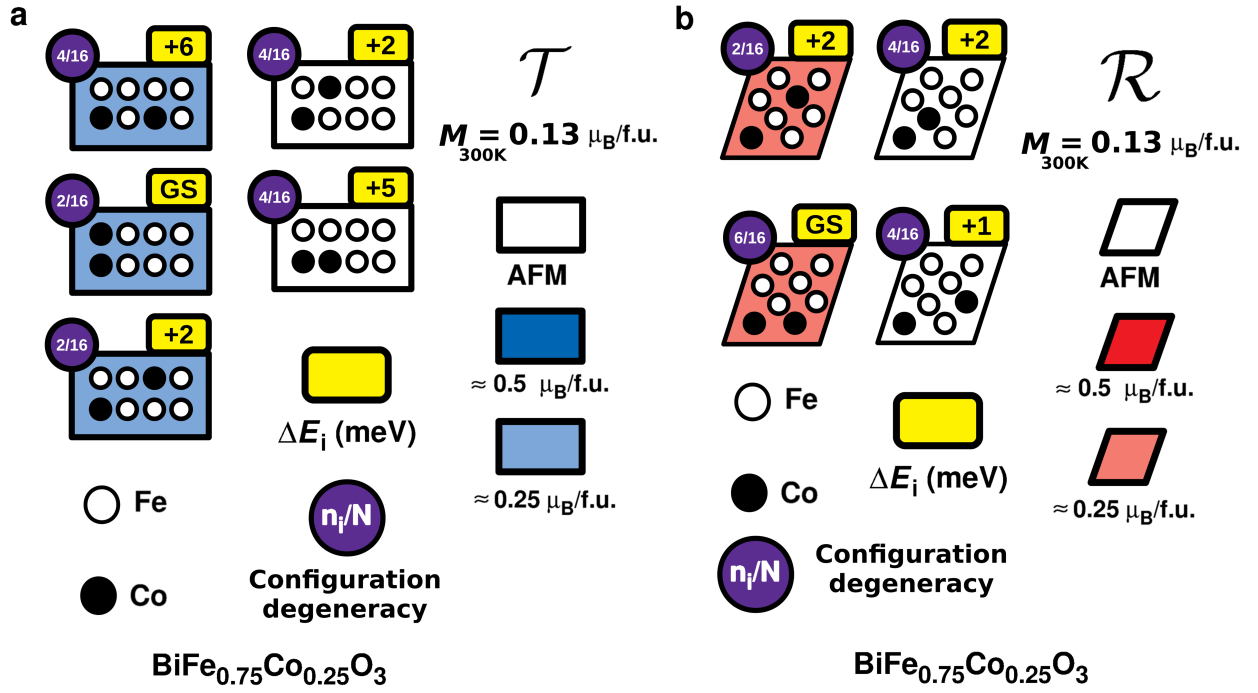
**Supplementary Figure 7:** (a) Total magnetization calculated by assuming thermal equilibrium conditions and configurational effects only (i.e., according to Eq.1 in the main text) and expressed as a function of temperature for the two most relevant crystal structures of bulk  $\text{BiFe}_{0.5}\text{Co}_{0.5}\text{O}_3$ . (b) Magnetic FiM  $\rightarrow$  PM (paramagnetic) transition temperatures estimated for the  $\mathcal{T}$  and  $\mathcal{R}$  phases expressed as a function of pressure. Results are obtained by performing Monte Carlo (MC) simulations of a spin Heisenberg model fitted to our data (Supplementary Methods). (c) Numerical value of the spin Heisenberg model parameters obtained in this study expressed as a function of pressure. (d) Example of MC simulation results obtained at a pressure of 1 GPa for the  $\text{BiFe}_{0.5}\text{Co}_{0.5}\text{O}_3$   $\mathcal{T}$  and  $\mathcal{R}$  phases.



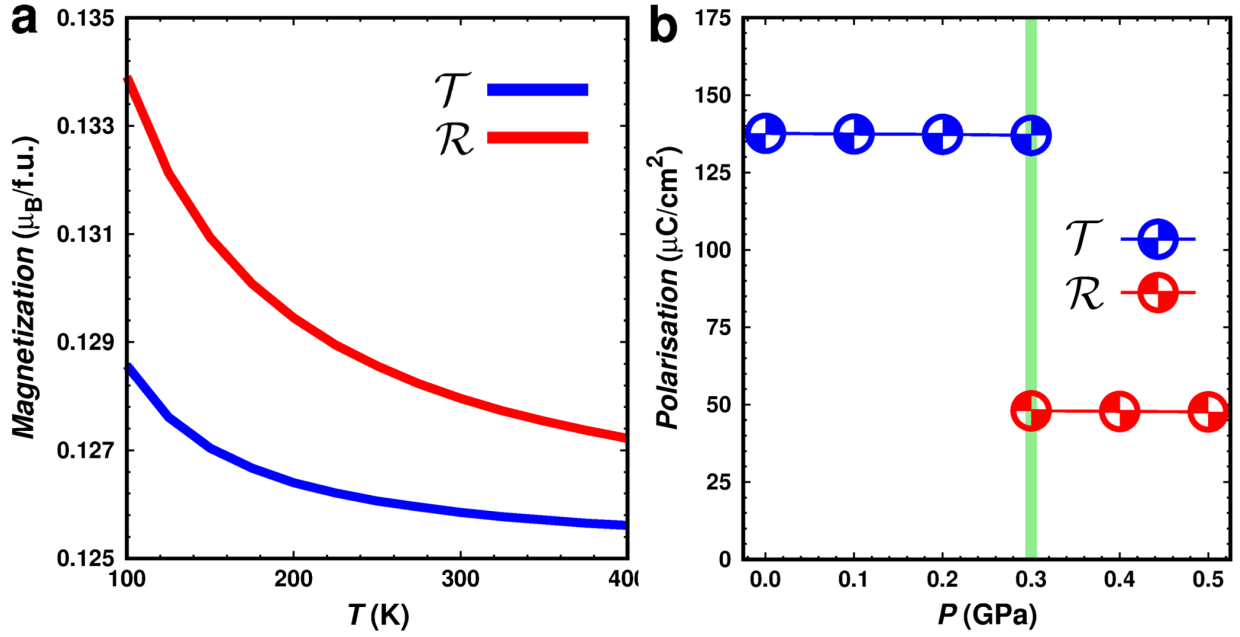
**Supplementary Figure 8:** Infrared intensity,  $I_{IR}$ , of the vibrational phonon modes calculated for bulk  $\text{BiFe}_{0.5}\text{Co}_{0.5}\text{O}_3$  for the relevant  $\mathcal{T}$  and  $\mathcal{R}$  phases and expressed as a function of the vibrational frequency. Vibrational phonon modes exhibiting  $I_{IR} \neq 0$  are polar whereas lattice excitations rendering null infrared intensities are non-polar. Non-polar phonon modes are more abundant at high vibrational frequencies, which are predominantly governed by oxygen atom displacements.



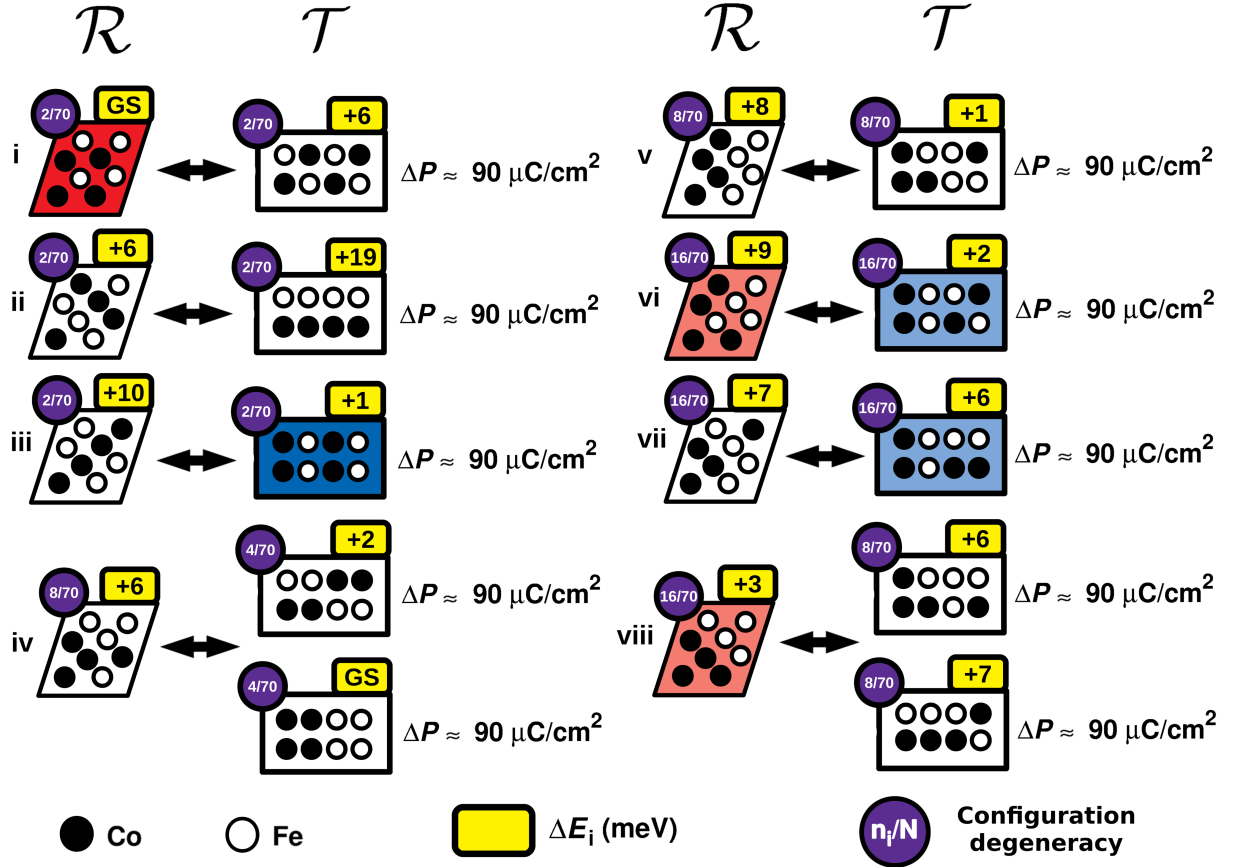
**Supplementary Figure 9:** Enthalpy energy differences calculated between several competing phases for bulk  $\text{BiFe}_{0.75}\text{Co}_{0.25}\text{O}_3$  at zero temperature and expressed as a function of pressure. A  $\mathcal{R}$  phase is stabilized over the  $\mathcal{T}$  ground state at a pressure of 0.3 GPa, which is 70% smaller than the analogous transition pressure calculated for bulk  $\text{BiFe}_{0.5}\text{Co}_{0.5}\text{O}_3$ . Results were obtained with the PBE DFT exchange-correlation energy functional [3].



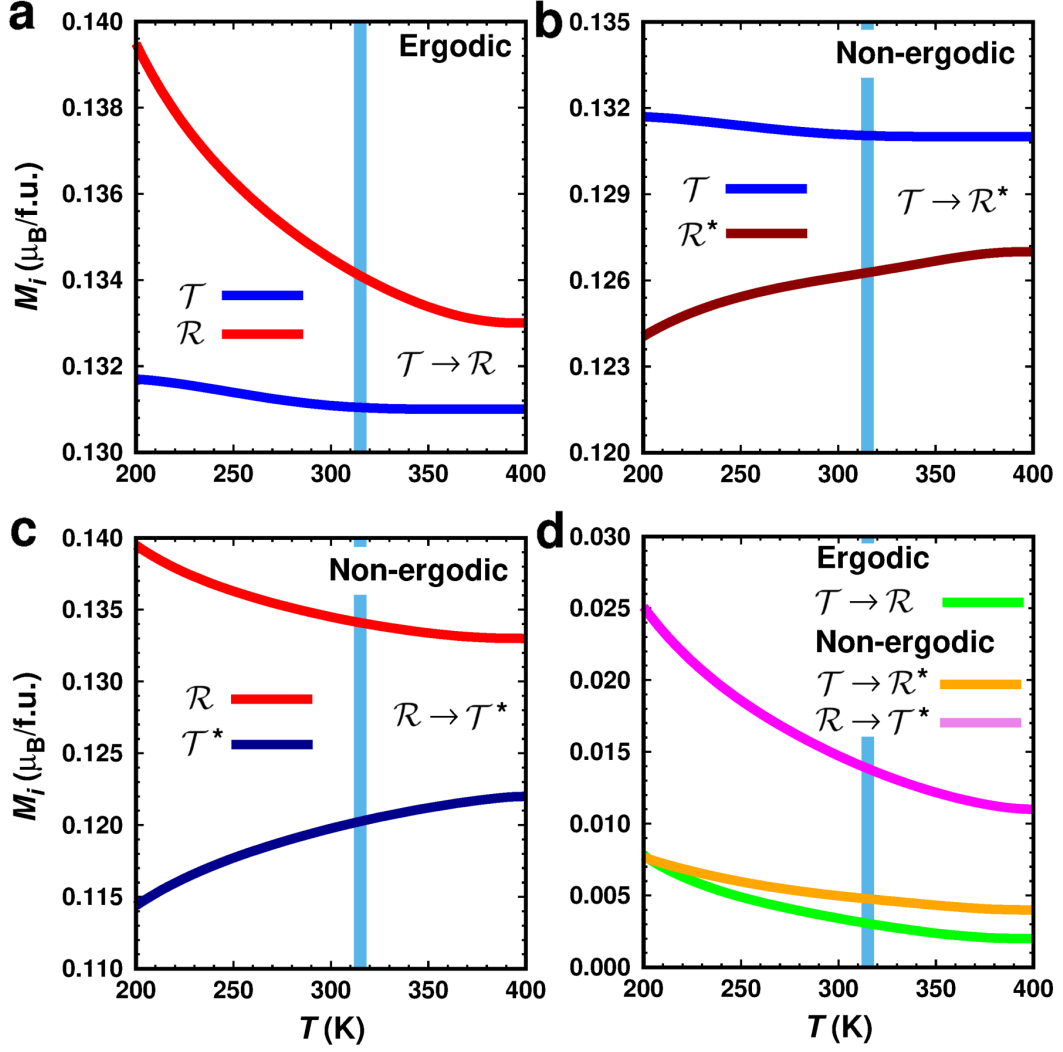
**Supplementary Figure 10:** First-principles determination of the magnetic properties of bulk  $\text{BiFe}_{0.75}\text{Co}_{0.25}\text{O}_3$  at finite temperatures for phases (a)  $\mathcal{T}$  and (b)  $\mathcal{R}$ . All possible atomic Co–Fe arrangements were generated for a  $2 \times 2\sqrt{2} \times \sqrt{2}$  simulation cell containing 40 atoms, which were reduced by crystal symmetry operations to 5  $\mathcal{T}$  and 4  $\mathcal{R}$  representative configurations [12]. The magnetic moment, total energy, and relative degeneracy of each representative configuration were calculated. The total magnetization estimated for each phase at room temperature is  $\approx 0.13 \mu_B$  per formula unit; “GS” stands for ground state and  $\Delta E_i \equiv E_i - E_{\text{GS}}$ .



**Supplementary Figure 11:** (a) Total magnetization calculated by assuming thermal equilibrium conditions and configurational effects only (Eq.1 in the main text) and expressed as a function of temperature for the two most relevant crystal structures of bulk  $\text{BiFe}_{0.75}\text{Co}_{0.25}\text{O}_3$ . (b) Electric polarization calculated with the Born effective charges method [4] and expressed as a function of pressure for the two most relevant crystal structures of bulk  $\text{BiFe}_{0.75}\text{Co}_{0.25}\text{O}_3$ . Calculation of the electric polarization was performed at  $T = 0$  conditions however, based on the experimental data reported by Azuma *et al.* [9,10], it is reasonable to expect that the estimated  $p$  values will not be affected noticeably by room-temperature thermal excitations.



**Supplementary Figure 12:** Analysis of the impact of non-ergodic cation redistribution effects on the  $\text{BiFe}_{0.5}\text{Co}_{0.5}\text{O}_3$  electric polarization features estimated by assuming ideal thermodynamic equilibrium conditions. The electric polarization estimated for each of the  $\mathcal{T}$  and  $\mathcal{R}$  configurations are very much similar among them, independently of the relative Co–Fe arrangements. Consequently, the change in electric polarization associated with the  $\mathcal{T} \leftrightarrow \mathcal{R}$  phase transformation is pretty robust, namely,  $\Delta p \approx 90 \mu\text{C}/\text{cm}^2$ , regardless of whether the Co and Fe ions can redistribute or not during the transition (Supplementary Discussion II). Electric polarization differences have been estimated with the Born effective charges approach [4].



**Supplementary Figure 13:** Analysis of the impact of non-ergodic cation redistribution effects on the  $\text{BiFe}_{0.5}\text{Co}_{0.5}\text{O}_3$  magnetic features estimated by assuming ideal thermodynamic equilibrium conditions. Total magnetizations are calculated by neglecting thermal excitations on magnetic ordering, that is, considering only configurational effects, and expressed as a function of temperature ( $P = 1.2$  GPa). (a) Thermal equilibrium, and thus ergodic, conditions are assumed. (b) Non-ergodic effects; relative Co–Fe cation arrangements are held fixed during the  $\mathcal{T} \rightarrow \mathcal{R}^*$  phase transformation, taken equal to those of the  $\mathcal{T}$  phase. (c) Non-ergodic effects; relative Co–Fe cation arrangements are held fixed during the  $\mathcal{R} \leftrightarrow \mathcal{T}^*$  phase transformation, taken equal to those of the  $\mathcal{R}$  phase. (d) Summary of the total magnetization changes estimated for the  $\mathcal{T} \leftrightarrow \mathcal{R}$  phase transformation when considering thermodynamic equilibrium conditions and non-ergodic effects (Supplementary Discussion II).

## SUPPLEMENTARY METHODS

### Spin Heisenberg model and details of the Monte Carlo simulations

To simulate the effects of thermal excitations on the magnetic ordering of  $\text{BiFe}_{0.5}\text{Co}_{0.5}\text{O}_3$   $\mathcal{T}$  and  $\mathcal{R}$ , we constructed several spin Heisenberg models of the form  $\hat{H} = \frac{1}{2} \sum_{ij} J_{ij} S_i S_j$  and performed Monte Carlo simulations with them. The value of the magnetic exchange constants involved in such spin models were obtained from zero-temperature DFT calculations, by following the approaches explained and already tested in previous works of ours [13–15].

In particular, for the  $\mathcal{T}$  phase ( $c > a$ ) we considered spin couplings between first nearest in-plane and out-of-plane neighbours ( $J_a$  and  $J_c$ , respectively) and between second nearest neighbours ( $J_{ac}$ ). The value of such magnetic exchange constants were obtained with the formulas [13–15]:

$$J_a^{\mathcal{T}} = \frac{1}{8|S|^2} (E^{\text{FM}} + E^{\text{A}} - E^{\text{C}} - E^{\text{G}}), \quad (1)$$

$$J_c^{\mathcal{T}} = \frac{1}{4|S|^2} (E^{\text{FM}} - E^{\text{A}} + E^{\text{C}} - E^{\text{G}}), \quad (2)$$

$$J_{ac}^{\mathcal{T}} = \frac{1}{16|S|^2} (E^{\text{FM}} - E^{\text{A}} - E^{\text{C}} + E^{\text{G}}), \quad (3)$$

where  $E$  represents energy and superscripts “FM”, “G”, “A”, and “C” ferromagnetic, antiferromagnetic G-type, antiferromagnetic A-type, and antiferromagnetic C-type spin arrangements, respectively (Supplementary Fig.1).

For the  $\mathcal{R}$  phase ( $c \approx a$ ), we considered only spin couplings between first nearest neighbours and obtained their value through the expression [13–15]:

$$J_a^{\mathcal{R}} = \frac{1}{6|S|^2} (E^{\text{FM}} - E^{\text{G}}). \quad (4)$$

The value of some magnetic exchange constants estimated by following the approach just described are reported in Supplementary Fig.7.

We used the spin Heisenberg models described above to perform Monte Carlo (MC) simulations in a periodically-repeated simulation box of  $20 \times 20 \times 20$  spins. Thermal averages were computed from runs of 50,000 MC sweeps after equilibration. These simulations allowed us to monitor the  $T$ -dependence of the magnetization through estimation of the magnetic C-type (for the  $\mathcal{T}$  phase) and G-type (for the  $\mathcal{R}$  phase) order parameters, namely,  $S^{\text{C}} \equiv \frac{1}{N} \sum_i (-1)^{n_{ix}+n_{iy}} S_{iz}$  and  $S^{\text{G}} \equiv \frac{1}{N} \sum_i (-1)^{n_{ix}+n_{iy}+n_{iz}} S_{iz}$  (Supplementary Fig.7). Here,

$n_{ix}$ ,  $n_{iy}$ , and  $n_{iz}$  are the three integers locating the  $i$ -th lattice cell, and  $N$  is the total number of spins in the simulation box. For the calculation of  $S^C$  and  $S^G$ , we considered only the  $z$  component of the spins because a small symmetry-breaking magnetic anisotropy was introduced in the Hamiltonian in order to facilitate the numerical analysis [13–15].

### Estimation of the electric polarization

For the estimation of the electric polarization,  $p$ , we employed the Berry phase formalism, which is regarded to be exact (besides ubiquitous numerical uncertainties) [5–7]. For these  $p$  calculations, we employed the range-separated hybrid functional HSE06 [8] and a total of 10 auxiliary system images for each phase and selected pressure (Supplementary Fig.3).

For comparison purposes, we also estimated the electric polarization perturbatively, that is, by employing the more straightforward Born effective charges approach [4]. In this case, the polarization is calculated with the formula:

$$p_\alpha = \frac{1}{\Omega} \sum_{\kappa\beta} Z_{\kappa\beta\alpha}^* u_{\kappa\beta} , \quad (5)$$

where  $\Omega$  is the volume of the cell,  $\kappa$  runs over all the atoms,  $\alpha, \beta = x, y, z$  represent Cartesian directions,  $\mathbf{u}_\kappa$  is the displacement vector of the  $\kappa$ -th atom as referred to a non-polar reference phase, and  $\mathbf{Z}_\kappa^*$  the Born effective charge tensor calculated for a non-polar reference state.

Supplementary Fig.3 shows the electric polarization results obtained for the  $\mathcal{T}$  and  $\mathcal{R}$  phases of  $\text{BiFe}_{0.5}\text{Co}_{0.5}\text{O}_3$  by employing the Berry phase formalism [5–7] and Born effective charges approach [4]. The electric polarization modules and electric polarization differences between the  $\mathcal{T}$  and  $\mathcal{R}$  phases are slightly and systematically larger when estimated with the exact Berry phase method. For instance, at the zero-temperature transition pressure we calculated 165 and 65  $\mu\text{C}/\text{cm}^2$  for the  $\mathcal{T}$  and  $\mathcal{R}$  phases with the Berry phase formalism (that is,  $\Delta p^{\text{Berry}} = 100 \mu\text{C}/\text{cm}^2$ ) and 140 and 50  $\mu\text{C}/\text{cm}^2$  with the Born effective charges method (that is,  $\Delta p^{\text{Born}} = 90 \mu\text{C}/\text{cm}^2$ ). On the other hand, the relative change in electric polarization for the  $\mathcal{T} \leftrightarrow \mathcal{R}$  phase transformation turns out to be somewhat higher when estimated with the Born effective charges approach, namely,  $\Delta p^{\text{Born}}/p^{\text{Born}} \approx 180\%$  and  $\Delta p^{\text{Berry}}/p^{\text{Berry}} \approx 150\%$ . Nevertheless, it can be concluded that the two methods provide electric polarization results that are in fairly good agreement.

## SUPPLEMENTARY DISCUSSIONS

### Supplementary Discussion I: On the role of the exchange-correlation DFT functional

The phase competition analysis for bulk  $\text{BiFe}_{0.5}\text{Co}_{0.5}\text{O}_3$  has been performed by considering three different DFT exchange-correlation approaches, namely, semi-local PBE+ $U$  [3] (Fig.1 in the main text), semilocal PBEsol+ $U$  [11] (Supplementary Fig.4) and the range-separated hybrid HSE06 [8] (Supplementary Fig.5). For the range-separated hybrid HSE06 analysis (Supplementary Fig.5), we have considered the equilibrium geometries determined with the semi-local PBE+ $U$  and PBEsol+ $U$  functionals. This combined DFT approach has been motivated by two facts; first, hybrid HSE06 geometry relaxations are computationally very intensive when employing plane-wave basis sets to describe electronic densities and orbitals, as it is our case (see technical DFT details in the main text); and second, the energies estimated for oxide perovskites with the hybrid HSE06 functional in general are quite insensitive to small structural variations (Supplementary Fig.5 and [16]).

The DFT energy results obtained with the hybrid HSE06 and semi-local PBE+ $U$  functionals are in excellent qualitative agreement and in fairly good quantitative agreement (Fig.1 in the main text and Supplementary Fig.5). Specifically, in both cases the  $\text{BiFe}_{0.5}\text{Co}_{0.5}\text{O}_3$  ground state is identified as  $\mathcal{T}$  with AFM-C spin ordering and the first metastable state as  $\mathcal{R}$  with AFM-G spin ordering. Also, the  $\mathcal{O}$  phase turns out to be energetically not competitive with the rest of phases. The estimated energy difference between the ground-state phase and the first metastable state, however, is noticeably larger in the hybrid HSE06 case (that is, approximately four times larger than calculated with the PBE+ $U$  functional). Meanwhile, the DFT energy results obtained with the semilocal PBEsol+ $U$  functional (Supplementary Fig.4) are in strong disagreement with both the hybrid HSE06 and semi-local PBE+ $U$  results. For instance, with the PBEsol+ $U$  functional the  $\text{BiFe}_{0.5}\text{Co}_{0.5}\text{O}_3$  ground state is identified as  $\mathcal{R}$  or  $\mathcal{M}$  with AFM-G spin ordering, since both phases are degenerate in energy within their numerical uncertainties. In addition, with the PBEsol+ $U$  functional (i) the energetically less favourable structure turns out to be the  $\mathcal{T}$  phase with AFM-C spin ordering, and (ii) the  $\mathcal{O}$  phase with AFM-G spin ordering turns out to be energetically competitive with the rest of phases.

It is worth mentioning that based on the agreement with the experimental data available for BFCO [9,10], the DFT results obtained with the hybrid HSE06 and semi-local PBE+ $U$  functionals appear to be the most reliable. For instance, the ground-state phase of  $\text{BiFe}_{0.5}\text{Co}_{0.5}\text{O}_3$  is experimentally identified as  $\mathcal{T}$  at any temperature below its decomposition point ( $\approx 900$  K) [9,10]. Also, orthorhombic phases are missing in the whole compositional BFCO phase diagram, thus indicating that they are not relevant for bulk at zero pressure. Based on all these comparisons, it is reasonable to expect that the results obtained with the semi-local PBE+ $U$  functional, which are the ones reported for BFCO in the main manuscript, are trustworthy.

**Supplementary Discussion II: On the role of possible non-ergodic cation redistribution effects occurring during the  $\mathcal{T} \leftrightarrow \mathcal{R}$  phase transformation**

Both Fe and Co cations are heavy weighted. Consequently, and since the temperatures considered in this study are relatively low ( $100 \leq T \leq 400$  K), it is possible that during the BFCO  $\mathcal{T} \leftrightarrow \mathcal{R}$  transformation the Co–Fe cations will remain quasi-static on their initial positions and thus will not follow the ideal thermal partition function given by Eq.(1) in the main text. In other words, in practice non-ergodic Co–Fe cation redistribution effects may exist during the  $\mathcal{T} \leftrightarrow \mathcal{R}$  phase transition. It seems then necessary to assess the likely impact of such non-ergodic effects on the main conclusions presented in the main text, namely, (1) the existence of a colossal variation in the electric polarization of  $\Delta p/p \sim 150\%$  during the  $\mathcal{R} \rightarrow \mathcal{T}$  transformation, and (2) the existence of robust magnetic  $\mathcal{T}$  and  $\mathcal{R}$  states at finite temperatures.

It is worth noting that at thermodynamic conditions other than the critical ones it is reasonable to expect that at least one of the two phases, either  $\mathcal{T}$  or  $\mathcal{R}$ , will follow the corresponding equilibrium thermal partition function (e.g., Eq.(1) in the main text). This condition implies that each possible configuration of the equilibrium phase (either  $\mathcal{T}$  or  $\mathcal{R}$ ),  $i$ , will occur in average according to the equilibrium probability  $w_i \equiv \exp(-\Delta E_i/k_B T)/Z_{\text{conf}}$ , where  $\Delta E_i \equiv E_i - E_0$ ,  $E_0$  is the ground-state energy,  $k_B$  the Boltzmann constant, and  $Z_{\text{conf}}$  the corresponding configurational partition function. In fact, such a condition can be somehow enforced in practice by employing adequate materials synthesis methods and protocols like, for instance, thermal treatment at high temperatures followed by annealing.

For simplification purposes, let us assume that we initiate the transformation, or series of back-and-forth transformations, from a  $\mathcal{T}$  phase that has been carefully prepared and thus it is statistically well represented by Eq.(1) in the main text. During the non-ergodic  $\mathcal{T} \rightarrow \mathcal{R}^*$  phase transition, the crystal is allowed to change its unit-cell volume and shape but the Co-Fe cations are not allowed to diffuse so as to rearrange. How these cation ordering constraints may affect our general findings (1) and (2)?

We started by establishing a “one-to-one” equivalence between all the  $\mathcal{T}$  and  $\mathcal{R}$  phase configurations that can be generated with the adopted 40-atoms simulation cell, based on their local Co-Fe coordination environment. Supplementary Fig.12 explicitly shows the equivalences that we established among the Co-Fe arrangements depicted in Fig.2 of the main text. Regarding the electric polarization, we found that the total and relative  $p$  differences between pairs of equivalent  $\mathcal{T}$  and  $\mathcal{R}$  configurations are always the same, namely,  $\Delta p^{\text{Born}} = 90 \mu\text{C}/\text{cm}^2$  and  $\Delta p^{\text{Born}}/p^{\text{Born}} \approx 180\%$  (as calculated with the Born effective charges approach [4]). This finding is a consequence of the fact that both Co and Fe cations contribute very similarly to the electric polarization (e.g., display practically identical Born effective charges), thus  $p$  is very insensitive to exchanges among Co-Fe cation positions. Therefore, independently of whether the Co-Fe cations can or cannot redistribute during the  $\mathcal{R} \rightarrow \mathcal{T}$  transformation, the resulting change in electric polarization will always be the same, namely, a giant  $\Delta p/p \sim 150\%$ .

Concerning the estimation of the saturated magnetization, our results obtained when considering non-ergodic cation redistribution effects are summarized in Supplementary Fig.13. In this case, non-ergodicity was modelled by adequately modifying the statistical weight (that is, factor  $w_i$ ) of each final phase configuration. In particular, we imposed that the statistical weight of each final phase (non-ergodic) configuration, let us say  $w_i^{\mathcal{R}^*}$ , is equal to the statistical weight of its equivalent initial phase (ergodic) configuration, that is,  $w_i^{\mathcal{R}^*} = w_i^{\mathcal{T}}$ . To be totally clear, for estimation of the “ergodic” saturated magnetization of, let us say, phase  $\mathcal{R}$  resulting from an ergodic  $\mathcal{T} \rightarrow \mathcal{R}$  transformation, we used the following formula (which is equivalent to Eq.(1) in the main text):

$$M_{\text{ergodic}}^{\mathcal{R}}(T) = \sum_i^{N_{\text{conf}}} w_i^{\mathcal{R}} \cdot M_i^{\mathcal{R}}, \quad (6)$$

whereas for estimation of the “non-ergodic” saturated magnetization of, let us say, phase

$\mathcal{R}^*$  resulting from an non-ergodic  $\mathcal{T} \rightarrow \mathcal{R}^*$  transformation, we used the formula:

$$M_{\text{non-ergodic}}^{\mathcal{R}^*}(T) = \sum_i^{N_{\text{conf}}} w_i^{\mathcal{R}^*} \cdot M_i^{\mathcal{R}} = \sum_i^{N_{\text{conf}}} w_i^{\mathcal{T}} \cdot M_i^{\mathcal{R}} . \quad (7)$$

As it is appreciated from Supplementary Figs.13a-b, the average magnetization estimated for the ergodic  $\mathcal{R}$  and non-ergodic  $\mathcal{R}^*$  phases are very similar and equal to  $\approx 0.13 \mu_B$  per formula unit.

Likewise, we considered the reverse non-ergodic transformation  $\mathcal{R} \rightarrow \mathcal{T}^*$ , which is initialized from a thermally equilibrated rhombohedral phase (Supplementary Fig.13c). In this case, the “non-ergodic” saturated magnetization of the  $\mathcal{T}^*$  phase can be estimated like:

$$M_{\text{non-ergodic}}^{\mathcal{T}^*}(T) = \sum_i^{N_{\text{conf}}} w_i^{\mathcal{T}^*} \cdot M_i^{\mathcal{T}} = \sum_i^{N_{\text{conf}}} w_i^{\mathcal{R}} \cdot M_i^{\mathcal{T}} . \quad (8)$$

The resulting saturated magnetization,  $\approx 0.12 \mu_B$  per formula unit (Supplementary Fig.13c), again is practically equal to the one estimated for the  $\mathcal{T}$  phase considering ergodic conditions, namely,  $\approx 0.13 \mu_B$  per formula unit (Supplementary Fig.13a).

The physical reasons for the similarity of the calculated ergodic and non-ergodic saturated magnetizations are that (i) the relative percentage of possible magnetic configurations are equal for both the  $\mathcal{T}$  and  $\mathcal{R}$  phases, namely,  $\approx 50\%$  (Fig.2 in the main text), and (ii) the energy difference for each configuration as referred to their corresponding ground state are in general very small, namely,  $\Delta E_i \sim 1 - 10 \text{ meV/f.u.}$  (Fig.2 in the main text), thus  $w_i^{\mathcal{R}} \approx w_i^{\mathcal{T}}$  for each pair of equivalent structures (Supplementary Fig.12).

Based on the results and discussions presented in this section, we may conclude that the likely existence of non-ergodic Co–Fe cation redistribution effects during the  $\mathcal{T} \leftrightarrow \mathcal{R}$  phase transformation will have a negligible effect on the main conclusions (1) and (2) presented in our manuscript.

## SUPPLEMENTARY REFERENCES

- <sup>1</sup> O. Diéguez and J. Íñiguez, *Phys. Rev. Lett.* **107**, 057601 (2011).
- <sup>2</sup> S. Prosandeev, D. Wang, W. Ren, J. Íñiguez, and L. Bellaiche, *Adv. Funct. Mater.* **23**, 234 (2013).
- <sup>3</sup> J. P. Perdew, K. Burke, and M. Ernzerhof, *Phys. Rev. Lett.* **77**, 3865 (1996).
- <sup>4</sup> C. Cazorla and M. Stengel, *Phys. Rev. B* **92**, 214108 (2015).
- <sup>5</sup> R. D. King-Smith and D. Vanderbilt, *Phys. Rev. B* **47**, 1651 (1993).
- <sup>6</sup> R. Resta, *Rev. Mod. Phys.* **66**, 899 (1994).
- <sup>7</sup> L. Bellaiche and D. Vanderbilt, *Phys. Rev. Lett.* **83**, 1347 (1999).
- <sup>8</sup> J. Heyd, G. E. Scuseria, and M. Ernzerhof, *J. Chem. Phys.* **118**, 8207 (2003).
- <sup>9</sup> M. Azuma, S. Niitaka, N. Hayashi, K. Oka, M. Takano, H. Funakubo, and Y. Shimakawa, *Jpn. J. Appl. Phys.* **47**, 7579 (2008).
- <sup>10</sup> H. Hojo, K. Oka, K. Shimizu, H. Yamamoto, R. Kawabe, and M. Azuma, *Adv. Mater.* **30**, 1705665 (2018).
- <sup>11</sup> J. P. Perdew, A. Ruzsinszky, G. I. Csonka, O. A. Vydrov, G. E. Scuseria, L. A. Constantin, X. Zhou, and K. Burke, *Phys. Rev. Lett.* **100**, 136406 (2008).
- <sup>12</sup> J. N. Shenoy, J. N. Hart, R. Grau-Crespo, N. L. Allan, and C. Cazorla, *Adv. Theory Simul.* **2**, 1800146 (2019).
- <sup>13</sup> C. Cazorla and J. Íñiguez, *Phys. Rev. B* **98**, 174105 (2018).
- <sup>14</sup> C. Cazorla and J. Íñiguez, *Phys. Rev. B* **88**, 214430 (2013).
- <sup>15</sup> C. Cazorla, O. Diéguez, and J. Íñiguez, *Sci. Adv.* **3**, e1700288 (2017).
- <sup>16</sup> K. T. Williams, L. K. Wagner, C. Cazorla, and T. Gould, arXiv:2005.03792 (2020).